Journal of The
Electrochemical Society

OPEN ACCESS

Probing the Influence of Steric Hindrance in Nonfluorinated Ether Electrolytes for Lithium Metal Batteries

To cite this article: Peiyuan Ma *et al* 2024 *J. Electrochem. Soc.* **171** 120536

View the article online for updates and enhancements.

You may also like

- Fast Charging of Energy-Dense Lithium Metal Batteries in Localized Ether-Based Highly Concentrated Electrolytes
  Yongjun Leng, Shanhai Ge, Xiao-Guang Yang et al.
- Influence of Lithium Metal Deposition on Thermal Stability: Combined DSC and Morphology Analysis of Cyclic Aged Lithium Metal Batteries
  L. Hellweg, T. Beuse, M. Winter et al.
- High Voltage Stable Li Metal Batteries Enabled by Ether-Based Highly Concentrated Electrolytes at Elevated Temperatures
  Yongjun Leng, Shanhai Ge, Ryan S. Longchamps et al.

PAT-Tester-x-8 Potentiostat:
Modular Solution for Electrochemical Testing!

EL-CELL®
electrochemical test equipment

✓ Flexible Setup with up to 8 Independent Test Channels!
Each with a fully equipped Potentiostat, Galvanostat and EIS!

✓ Perfect Choice for Small-Scale and Special Purpose Testing!
Suited for all 3-electrode, optical, dilatometry or force test cells from EL-CELL.

✓ Complete Solution with Extensive Software!
Plan, conduct and analyze experiments with EL-Software.

✓ Small Footprint, Easy to Setup and Operate!
Usable inside a glove box. Full multi-user, multi-device control via LAN.

Scan me!

Contact us:
☎ +49 40 79012-734
✉ sales@el-cell.com
🌐 www.el-cell.com

This content was downloaded from IP address 73.9.102.34 on 09/05/2025 at 03:21

Journal of The Electrochemical Society, 2024 **171** 120536

Probing the Influence of Steric Hindrance in Nonfluorinated Ether Electrolytes for Lithium Metal Batteries

Peiyuan Ma, Uyen Le, Ke-Hsin Wang, Minh Canh Vu, Priyadarshini Mirmira, and Chibueze V. Amanchukwu[*,z]

Pritzker School of Molecular Engineering, University of Chicago, Illinois 60637, United States of America

Lithium metal batteries (LMBs), especially "anode-free" LMBs, promise much higher energy density than current lithium-ion batteries but suffer from poor capacity retention. While novel electrolytes have been designed to extend cycle life in anode free LMBs, most of them contain a high fraction of fluorinated solvents or diluents that may cause environmental concerns. Herein, we report the design and synthesis of a group of nonfluorinated ether solvents (termed xME solvents). By substituting the methyl terminal group of 1,2-dimethoxy ethane (DME) with different alkyl groups, the solvation power of xME solvents was tuned to be weaker, leading to more ion pairing in electrolyte solvation structure. In anode free type Cu/$LiFePO_4$ (Cu/LFP) cells, xME electrolytes in general show better capacity retention than DME-based electrolyte. Some xME electrolytes also show better oxidative stability than DME against aluminum and $LiNi_{0.8}Mn_{0.1}Co_{0.1}O_2$ (NMC811) electrodes. While the general improvement in LMB cycle life and oxidative stability can be attributed to more ion pairing, the local variation within xME electrolytes indicates other factors are also important. Our work proposes a molecular design strategy to fine-tune ion solvation structure of nonfluorinated ether electrolytes for LMBs.

[DOI: 10.1149/1945-7111/ad9cca]

Manuscript submitted September 23, 2024; revised manuscript received November 18, 2024. Published December 26, 2024.

Supplementary material for this article is available online

Lithium-ion batteries (LIBs) have dominated the consumer electronic market and are powering the rapidly expanding electric vehicle market.[1] However, current LIBs may not meet the ever-growing energy density requirements. To break the practical energy density limit of intercalation electrodes, conversion chemistries based on lithium metal and alloy anodes such as silicon and tin, are highly desired.[2] Among them, the lithium metal anode has attracted great research interest because of its high theoretical specific capacity and low electrochemical potential.[3] Pairing lithium metal anode with state-of-the-art layered oxide cathodes, lithium metal batteries (LMBs) can theoretically achieve ∼50% higher energy density than LIBs.[2] Nonetheless, to fully realize the potential of lithium metal anode, capacity ratio between negative electrode and positive electrode has to be kept low in practical LMBs or the so called "anode free" configuration with no excess lithium should be adopted.[4,5] In practical LMBs with limited or no lithium reservoir, the high chemical reactivity and low deposition/stripping reversibility of lithium metal leads to rapid capacity decay.[5–7] Therefore, mitigating capacity loss and extending cycle life are grand challenges for LMBs.

Different approaches, including current collector engineering, cycling condition optimization and electrolyte engineering have been explored to improve the cycling behavior of anode free LMBs.[5] Among them, electrolyte engineering has attracted great interest since it allows the modification of the solid electrolyte interphase (SEI), which has been widely believed to play a key role in modulating lithium metal cycling stability.[8–10] Several novel electrolytes have been reported in recent years. Among them, localized high concentration electrolytes (LHCEs) utilize a high salt to solvent molar ratio and non-solvating fluoroether diluents to achieve a solvation structure rich in anion, which is proposed to induce an anion-derived SEI and improve cycle life of anode free LMBs.[11] Besides, electrolytes composed of fluoroethylene carbonate (FEC), diethyl carbonate (DEC), lithium difluoro(oxalato)borate (LiDFOB) and $LiBF_4$ are also reported to enable long cycle life anode free LMBs.[4,12] The LiDFOB and $LiBF_4$ salts are reported to have a synergistic effect that leads to a favorable lithium deposition morphology. Recently, fluorinated ether solvent based electrolytes have been developed and optimized for anode free LMBs, where the high lithium metal Coulombic efficiency and long cycle life are also attributed to a solvation structure rich in anionic species and consequently an anion-derived SEI.[13,14]

While the success of those electrolytes is usually attributed to ion pairing and anion-derived SEI, the exact correlation between ion solvation structure to lithium metal cycling efficiency has not been fully explored. Moreover, the role of reactive or potentially reactive solvent (FEC or fluorinated ethers) in SEI construction remains unclear, which makes mechanistic elucidation difficult.[15–18] In addition, the above mentioned electrolytes all contain a significant volume fraction of fluorinated solvent/diluent, which may lead to additional environmental cost such as PFAS (per- and poly-fluoroalkyl substances) hazard in their life cycle.[19,20] In comparison to fluorinated compounds, nonfluorinated ether compounds are known for their high reductive stability and possess less environmental concerns.[1] Recently, several weakly solvating nonfluorinated ether solvents have been investigated for LMBs.[21–25] While high lithium metal Coulombic efficiency and improved oxidative stability are reported, only few nonfluorinated ether electrolytes were tested in anode free LMBs. In addition, most studies are based on the limited number of commercially available compounds, and the molecular structure of nonfluorinated ether has not been fine-tuned. Therefore, it is desired to further explore the chemical space of nonfluorinated ether solvents from a mechanistic perspective.

In this work, we design and synthesize a group of asymmetric and sterically hindered nonfluorinated ether solvents structurally modified from 1,2-dimethoxy ethane (DME). By replacing the methyl group with different alkyl groups, steric hindrance is introduced in the molecular structure to tune solvation power. We show that while increased steric hindrance promotes ion pairing in electrolyte solvation structure, overly high steric hindrance leads to undesired phase separation. Owing to promoted ion pairing in solvation structure, the sterically hindered nonfluorinated ethers (termed xMEs) in general leads to improved cycle life in anode free Cu/$LiFePO_4$ (Cu/LFP) cells compared to DME. However, local variance within them indicates solvation structure might not be the only determining factor. We also show that some xME electrolytes have better oxidative stability than DME and can enable longer cycle life in Li/$LiNi_{0.8}Mn_{0.1}Co_{0.1}O_2$ (Li/NMC811) cells. Our work explores new chemical space of

---

[*] Electrochemical Society Member.

[z] E-mail: chibueze@uchicago.edu

nonfluorinated ether solvents and elucidates the effect of steric hindrance on solvent solvation power and electrolyte properties.

Results and Discussion

Molecular design and synthesis.—A series of asymmetric and increasing bulky nonfluorinated ether solvents were synthesized to probe the influence of steric hindrance on ion transport and subsequent electrochemistry. As shown in Fig. 1, 1,2-dimethoxy ethane (DME) is a widely studied nonfluorinated ether solvent. Due to its strong solvation power, DME can fully dissociate lithium salt at dilute concentrations (~1 M). To decrease the solvation strength of DME and promote ion pairing, we design and synthesize a set of asymmetric ethers where one of the methyl groups of DME is replaced by longer alkyl chains that induce more steric hindrance. With substitution of isopropyl, isobutyl, *n*-butyl and cyclopentyl groups, the resultant new compounds are termed as isopropyl 2-methoxyethyl ether (iPrME), isobutyl 2-methoxyethyl ether (iBME), *n*-butyl 2-methoxyethyl ether (nBME) and cyclopentyl 2-methoxyethyl ether (cPME), respectively. As discussed later, these modified DME solvents (termed xMEs) can dissolve 1 M lithium bis(fluorosulfonyl)amide (LiFSA) salt and lead to more ion pairing in their solvation structure. To further promote ion pairing, DME-derived compounds with both methyl groups substituted by longer alkyl groups were also designed and synthesized. However, they lead to phase separation when preparing "1 M" LiFSA solution as shown in Fig. S1. Although phase separation can be avoided at higher salt concentration (Table S1), we focus on the four xME solvents that can form stable 1 M LiFSA solutions in this work (Fig. 1).

The xME family compounds were synthesized by one-step reactions between corresponding precursors as shown in Fig. S2. iPrME, iBME and nBME were synthesized by reacting corresponding ethylene glycol mono-alkyl ether with iodomethane using sodium hydride as base. For cPME, the synthesis reaction was performed with bromo cyclopentane, 2-methoxy ethanol and sodium carbonate. The structure and product purity were verified using ^{1}H and ^{13}C nuclear magnetic resonance (NMR) spectroscopy (See supporting information).

Ion solvation structure.—The ion solvation structure in these asymmetric nonfluorinated ether electrolytes was investigated by electrochemical and spectroscopic techniques. Figure 2a shows the Raman peak of FSA anion in 1 M LiFSA solutions. Compared to DME, the FSA$^-$ peak generally shifts to higher wavenumbers in xME electrolytes, indicating an increase in ion pairing.[26] The fraction of different solvation environments can be estimated by fitting the FSA peak with three components: solvent-separated ion pair (SSIP); contact-ion pair (CIP) and salt aggregates (AGG).[27] Within xME electrolytes, the solvation environment in iBME and nBME is dominated by CIP (53% and 49%) while iPrME and cPME have relatively higher fraction of SSIP (48% and 41%). Figure 2b shows cyclic voltammetry (CV) curves of 1 M LiFSA in nonfluorinated ether electrolytes containing 1 mM ferrocene (Fc) in lithium/platinum (Li/Pt) cell, following the protocol recently reported by Yamada et al.[28] Assuming a constant potential of Fc/Fc$^+$ as the reference, Li/Li$^+$ potentials (E_{Li}) in different electrolytes can be calculated and serve as an indicator of ion solvation structure. Compared to DME ($E_{\mathrm{Li}} = -3.40$ V), xME electrolytes show clearly increased E_{Li} values (less reductive potentials), which indicates weaker Li$^+$ solvation environment and more ion pairing. However, the trend within xME electrolytes is weak: From the lowest nBMEE ($E_{\mathrm{Li}} = -3.34$ V) to the highest iBMEE ($E_{\mathrm{Li}} = -3.31$ V), the 0.03 V difference is almost negligible in comparison to the full range of E_{Li} (-3.5 V ~ -2.9 V).[28] As summarized in Fig. 2c, both Raman spectroscopy and E_{Li} results support increased ion pairing in xMEs in comparison to DME. However, the correlation within xME electrolytes is not monotonic and no clear order can be drawn, which also suggests the differences within xME electrolytes might be subtle. We should also note that xME electrolytes have relatively less ion pairing compared to strong ion pairing systems such as high concentration electrolytes and fluorinated ether electrolytes.[27,29,30]

Ion transport properties.—Ionic conductivity in the nonfluorinated ether electrolytes was probed using electrochemical impedance spectroscopy (EIS) and correlated to viscosity and ion solvation structure. Figure 3a shows the ionic conductivity of 1 M LiFSA in nonfluorinated ether solvents as a function of temperature.

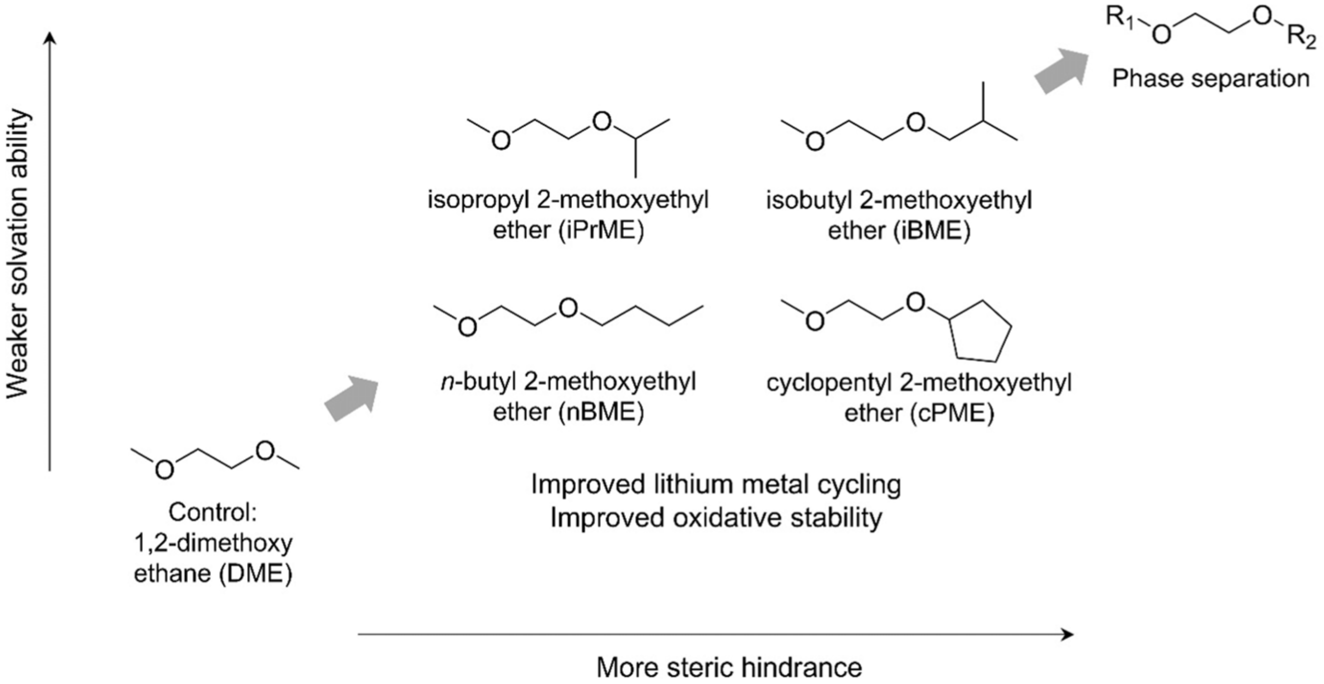

Figure 1. Molecular design strategy. As a widely studied nonfluorinated ether solvent, 1,2-dimethoxy ethane (DME) has good reductive stability but moderate lithium metal cycling stability due to lack of ion pairing. To promote a solvation structure rich in ion pairing, one of the methyl end groups of DME is replaced by longer alkyl group to increase steric hindrance. Further increasing steric hindrance by replacing both methyl groups with longer alkyl groups results in phase separation when salt is dissolved at 1 M concentration, indicating inadequate solvation ability.

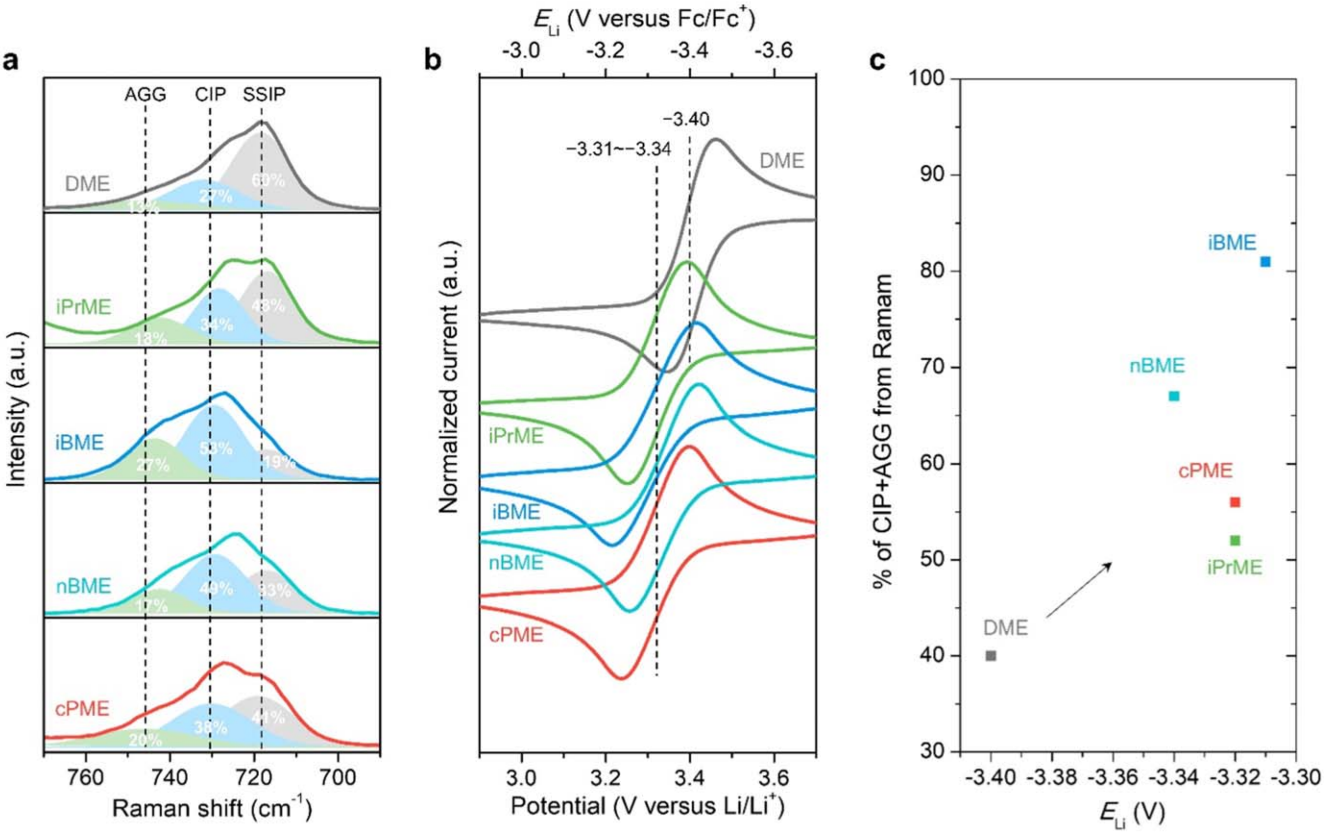

Figure 2. Ion solvation structure. (**a**) Raman spectroscopy of FSA anion in 1 M LiFSA/ nonfluorinated ether solutions. SSIP: solvent-separated ion pair; CIP: contact-ion pair; AGG: salt aggregates. (**b**) Lithium redox potential (E_{Li} referenced to $\mathrm{Fc/Fc^{+}}$) in 1 M LiFSA in nonfluorinated ether electrolytes. (**c**) Summary of different measurements of ion solvation structure. Both Raman spectroscopy and E_{Li} show increased ion pairing from DME to modified xME electrolytes. Fc = Ferrocene.

At room temperature (20 °C), ionic conductivity decreases in the order of DME (9.96 mS $\mathrm{cm^{-1}}$), iPrME (6.22 mS $\mathrm{cm^{-1}}$), nBME (3.70 mS $\mathrm{cm^{-1}}$), iBME (3.35 mS $\mathrm{cm^{-1}}$) and cPME (2.93 mS $\mathrm{cm^{-1}}$). As shown in Fig. S3, activation energy barrier of ion transport increases in the same order as extracted from the Arrhenius fitting of conductivity data. At lower temperature, iPrME and iBME electrolytes show turning points after which conductivity drops rapidly, which is likely due to phase transition as supported by differential scanning calorimetry (DSC) results shown in Fig. S4. To understand the trend in conductivity, the viscosity of nonfluorinated ether electrolytes was measured. As shown in Fig. 3b, viscosity increases in order of DME (1.58 mPa s), iPrME (1.71 mPa s), iBME (2.36 mPa s), nBME (2.52 mPa s), cPME (3.98 mPa s), which roughly correlates to increasing solvent molecular weight. Walden plot shown in Fig. 3c reveals that ionic conductivity of nonfluorinated ether electrolytes in general follows viscosity trend. However, their correlation is not linear, especially for DME, due to effects of the ion solvation structure. By comparing to the diagonal fully

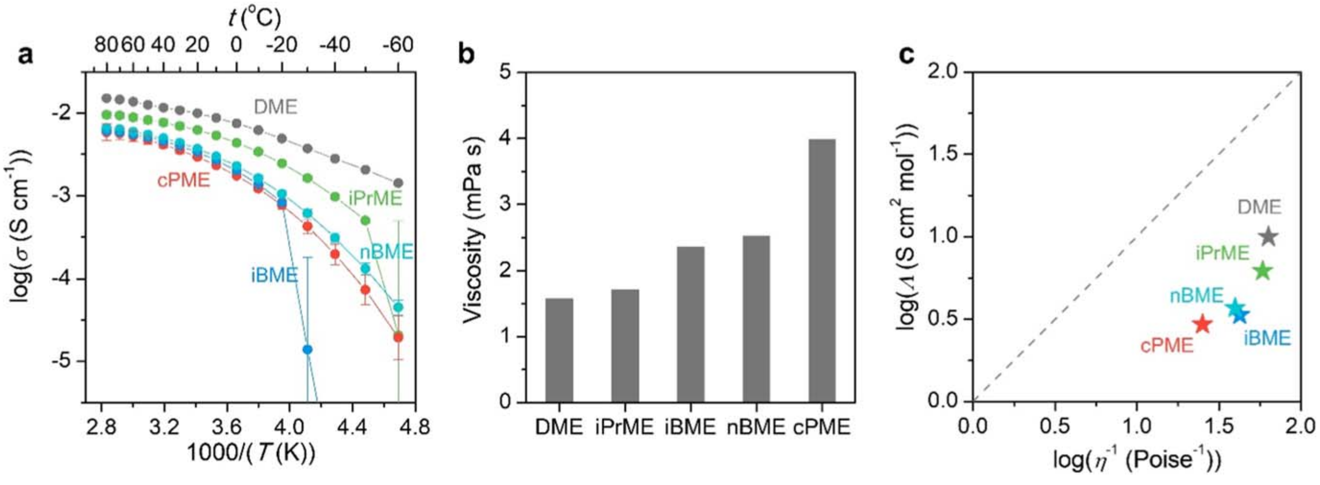

Figure 3. Ion transport. (**a**) Ionic conductivity as a function of temperature of 1 M LiFSA in nonfluorinated ether electrolytes. Conductivity values are averaged from three measurements and error bar represents standard deviation. The lines are to guide the eyes. (**b**) Viscosity of 1 M LiFSA in nonfluorinated ether electrolytes. (**c**) Walden plot of 1 M LiFSA in nonfluorinated ether electrolytes that correlates ionic conductivity to viscosity. The diagonal dash line indicates fully dissociated electrolytes (aqueous solution of KCl).

dissociated electrolyte line (KCl aqueous solution),[31] the degree of ionicity can be quantified, where DME shows a significantly higher ionicity degree (15.7%) than the modified xMEs (10.7%, 7.9%, 9.3% and 11.7% for iPrME, iBME, nBME and cPME, respectively). The lower degree of ionicity in xME electrolytes agrees with their solvation structure rich in ion pairing as discussed earlier. The ion diffusivity and lithium transference number in xME electrolytes were also studied by Pulsed Field Gradient Nuclear Magnetic Resonance (PFG NMR) spectroscopy. As shown in Fig. S5, ion diffusivity decreases from DME to cPME, following increasing viscosity. Due to more ion pairing in their ion solvation structure, xME electrolytes show slightly higher lithium transference number than DME electrolyte.

Lithium metal cycling stability.—The lithium metal compatibility of the nonfluorinated ether electrolytes was studied in Cu/LFP and Li/Cu cells. Figure 4a shows the discharge capacity and Coulombic efficiency of Cu/LFP cells cycled at a constant current rate of C/3 (1 C ≈ 1.77 mA cm^{-2}) after two formation cycles at C/10. Compared to DME electrolyte, iPrME, iBME and nBME electrolytes have better capacity retention and more stable Coulombic efficiency. cPME electrolyte also shows stable capacity retention but has lower discharge capacity than DME due to poor initial cycle Coulombic efficiency. The best performing iPrME electrolyte maintains 62% of initial discharge capacity at 60th cycle (relative to the 1st C/3 cycle discharge capacity and averaged from two cells) followed by iBME and nBME that maintain 55% and 54% of initial capacity, respectively. In contrast, the Cu/LFP cells using DME electrolyte can only maintain 32% of initial capacity after 60 cycles. Lithium metal cycling efficiency was also evaluated in Li/Cu half cells following the Aurbach method as shown in Fig. 4b.[32] Within xME electrolytes, the Aurbach method Coulombic efficiency decreases in order of iPrME (99.1%), nBME (97.8%), iBME (97.7%) and cPME (94.5%), which matches the capacity retention trend in Cu/LFP cell. Interestingly, DME shows a high Coulombic efficiency of 98.5% that conflicts with its poor capacity retention in Cu/LFP cell. Since similar Coulombic efficiency and anode free cell cycling performance have been reported in literature,[13] the discrepancy between Li/Cu and anode free cell might be due to cell configuration differences and the limited cycle number of the Aurbach method. Hence, cycling of anode free cell or full cell with limited excess lithium metal might be necessary to precisely evaluate electrolyte performance in LMBs.

As a representation of good performing xME electrolytes, the lithium deposition morphology in the best performing iPrME electrolyte was studied by scanning electron microscopy (SEM) and compared to DME to understand their contrast in anode free cell cycling performance. Figures 4c and 4d show the SEM images of lithium metal deposited in Cu/LFP cells at C/3 to 3.8 V (∼2 mAh cm^{-2}) after two formation cycles at C/10 (the same protocol as long term cycling). Compared to DME, iPrME leads to less fraction of small dendrites in the top morphology of deposited lithium metal. As shown in Figs. 4e and 4f, the cross section SEM images indicate that lithium deposited in iPrME electrolyte has lower thickness and more compact structure in comparison to lithium deposited in DME electrolyte. In addition, digital photos shown in Fig. S6 reveal that iPrME electrolyte produces more uniform distribution of lithium deposits on Cu current collector while lithium deposits are more clustered in DME electrolyte, which suggests more uniform current distribution and lower local current density in iPrME electrolyte.

Since it is widely believed that lithium deposition morphology is strongly affected by solid electrolyte interphase (SEI) properties,[8–10] SEI composition in nonfluorinated ether electrolytes was probed by X-ray photoelectron spectroscopy (XPS). However, Fig. S7 shows

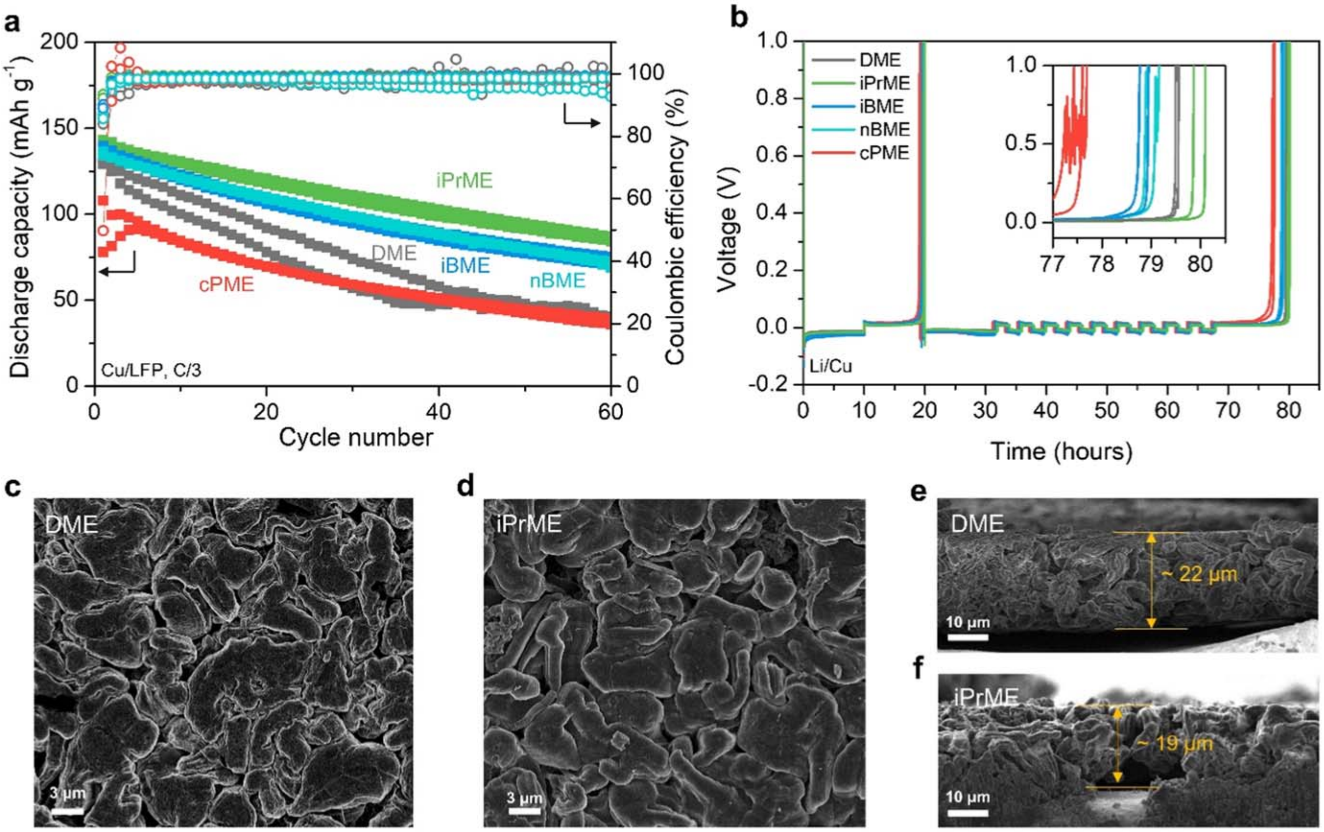

Figure 4. lithium metal cycling performance. (**a**) Cycling performance of nonfluorinated ether electrolytes in Cu/LFP cells. (**b**) Lithium metal cycling Coulombic efficiency measurement in Li/Cu cells following the Aurbach method. Two replicates are shown for each electrolyte. (**c**)–(**d**) SEM images of lithium metal deposition morphology in Cu/LFP cells using (**c**) 1 M LiFSA in DME electrolyte and (**d**) 1 M LiFSA in iPrME electrolyte. (**e**)–(**f**) Cross section SEM images of lithium metal deposited in Cu/LFP cells using (**e**) 1 M LiFSA in DME electrolyte and (**f**) 1 M LiFSA in iPrME electrolyte.

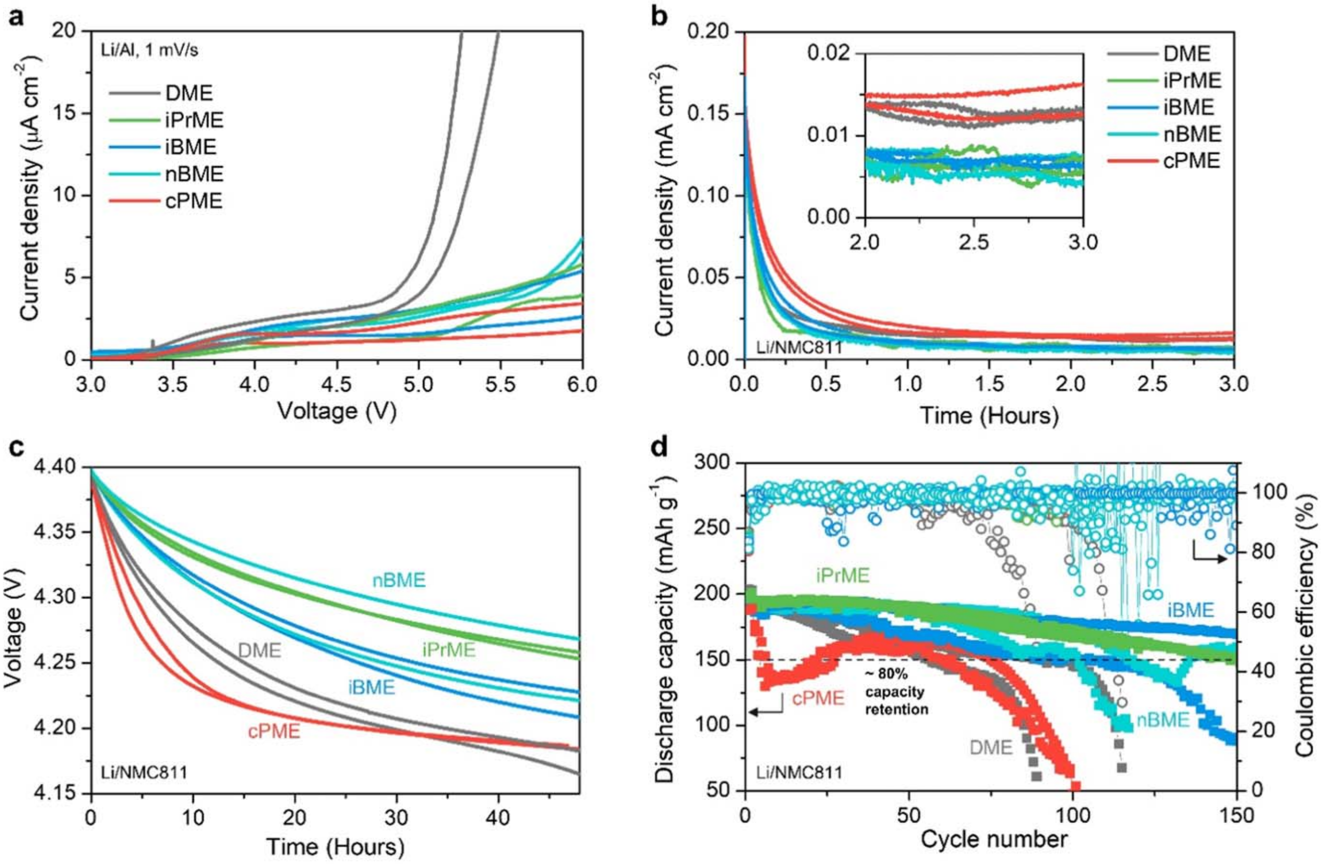

Figure 5. Oxidative stability. (**a**) Linear sweep voltammetry (LSV) of 1 M LiFSA in nonfluorinated ether electrolytes in Li/Al cells. (**b**) Chronoamperometry of nonfluorinated ether electrolytes in Li/NMC811 cells at a constant potential of 4.4 V vs Li/Li$^+$. (**c**) Self-discharging of Li/NMC811 cells after chronoamperometry test at 4.4 V. (**d**) Cycling of Li/NMC811 cells at a current rate of C/10 after two formation cycles at C/10. 1 C ≈ 1.66 mA cm^{-2}. Two replicates are shown for each test.

no obvious difference between iPrME and DME in SEI composition, especially for inorganic components such as LiF and Li_2O. As another popular descriptor for lithium metal compatibility,[28,33] ion solvation structure of the studied nonfluorinated ether electrolyte was also correlated to anode free cell cycling performance. As shown in Fig. S8, the increased ion pairing in xME electrolytes could be correlated to their better cycling performance compared to DME, but solvation structure fails to explain performance variability within the xME electrolytes. Therefore, while the performance of xME electrolytes still support ion pairing as an important criterion for anode free LMB electrolyte design,[14,28,33] other descriptors are needed and will be investigated in future studies.

Oxidative stability.—Since poor oxidative stability is one of the major weaknesses of conventional ether electrolytes, [1] improving oxidative stability is set as a target in many previously published nonfluorinated ether design.[21–25] Therefore, the oxidative stability of xME electrolyte was also tested on aluminum and NMC811 working electrodes and the influence of substitution group was investigated. Figure 5a shows linear sweep voltammetry (LSV) curves of nonfluorinated ether electrolytes in Li/Al cells, where DME electrolyte has a rapid current density rise around 4.8 V, which indicates instability against aluminum (and inability to passivate) at higher voltage. In contrast, xMEs electrolyte all show flat LSV curves up to 5.7 V with current density less than 5 μA cm^{-2}, illustrating their improved stability against aluminum working electrode. To evaluate the stability of nonfluorinated ether electrolytes against Ni-rich NMC811 cathode, they were tested in Li/NMC811 cells by first charging to 4.4 V at C/10 and then holding at 4.4 V for 3 h. Figure 5b shows that during the 3 h potentiostatic hold at 4.4 V, iPrME, iBME and nBME electrolytes have leakage current density lower than DME and cPME electrolytes. This indicates iPrME, iBME and nBME lead to less parasitic reaction and better stability with NMC811 cathode. In the following self-discharging test shown in Fig. 5c, iPrME, iBME and nBME exhibit slower self-discharge rate with terminal voltage above 4.2 V after 48 h while DME and cPME show faster self-discharging with cell voltage dropping below 4.2 V in 48 h. The self-discharging test corroborates the leakage current density trend and supports that iPrME, iBME and nBME have better oxidative stability than DME and cPME against NMC811 cathodes. Since DFT calculations show little variation in oxidation potential among DME and xME molecules (Fig. S9), the experimentally observed oxidative stability trend might be due to different interfacial passivation ability.

The effect of oxidative stability on cycling stability was studied in long term cycling of Li/NMC811 cells. As shown in Fig. 5d, iPrME, iBME and nBME electrolytes enable long cycle life of 110 ~ 150 cycles in Li/NMC811 cells before their capacity drops below 80% of initial capacity, in agreement with potentiostatic hold and self-discharging test results. By contrast, DME and cPME electrolytes show poorer Li/NMC811 cell cycle life of 60 ~ 100 cycles. In addition, cPME electrolyte has unstable discharge capacity in the initial cycles of Li/NMC811 cell, also indicating poor stability against NMC811 electrode.

Conclusions

In this work, we probe the influence of steric hindrance in nonfluorinated ether electrolytes for anode free LMBs. By replacing one methyl group of DME with longer alkyl groups, the solvation ability of resultant xME solvents is weakened due to increased steric hindrance. Further increasing steric hindrance by adding longer alkyl groups to both ends of ethylene glycol backbone leads to phase separation in electrolyte solution. With reduced solvation ability, xME solvents promotes more ion pairing in the solvation structure compared to DME. In anode free type Cu/LFP cell, xME electrolytes show better cycle life than DME electrolyte due to compact and uniform lithium deposition morphology. Furthermore, xME electrolytes also show improved oxidative stability against aluminum or NMC811 working electrodes. While increased ion pairing from DME to xMEs in general correlates to the improvement in lithium metal cycling and oxidative stability, other factors are needed to explain the performance variance among xMEs. The molecular design principles illustrated in this work will help facilitate the development of sustainable electrolytes for anode free LMBs.

Experimental

Materials.—DME (anhydrous, inhibitor free, 99.8%), sodium hydride (60% in mineral oil), diethyl ether, iodomethane and 4 Å molecular sieves were purchased from Sigma-Aldrich. Ethylene glycol mono-*n*-butyl ether, ethylene glycol mono-*iso*-butyl ether, and ethylene glycol mono-*tert*-butyl ether were purchased from TCI America. Ethylene glycol mono-*iso*-propyl ether, tetraethylene glycol dimethyl ether (tetraglyme), cyclopentyl bromide, 1-iodobutane, 2-methoxyethanol, ethyl p-toluenesulfonate, and magnesium sulfate (anhydrous), ethyl acetate (EA, HPLC grade) and hexanes were purchased from Fisher Scientific. Lithium bis(fluorosulfonyl) amide (LiFSA) was purchased from Arkema. Deuterated solvents (⩾99.8 atom % D) were purchased from Cambridge Isotope Laboratories.

Celgard 2325 separator was purchased from Celgard LLC. Separator was cut into 18 mm diameter disks and vacuum dried at 70 °C overnight before use. All CR2032 coin cell parts were obtained from Xiamen TOB New Energy Technology. Lithium foil (500 μm thick) was purchased from China Energy Lithium. Lithium foil was polished with a brush to remove oxide layer and cut into 12 mm diameter disks before use. LFP and NMC811 electrodes were kindly provided by Cell Analysis, Modeling, and Prototyping (CAMP) facility of Argonne National Laboratory. The specifications of electrodes can be found in Table S2. Electrodes were cut into 12 mm diameter disks and vacuum dried at 120 °C overnight in a heated glovebox antechamber before use.

Synthesis.— *Synthesis of iPrME, iBME, nBME, iPrEE and tBEE.*—In the example of nBME, 150 ml dry tetraglyme was added to a round bottom flask followed by 5.08 g (1.2 eq.) NaH (60 wt% separated in mineral oil) under nitrogen protection. The suspension was cooled by ice batch to 0 °C and 13.76 g (1.1 eq.) ethylene glycol mono-*n*-butyl ether was added dropwise. The mixture was stirred for 2 h from 0 °C to room temperature. 15.02 g (1.0 eq.) iodomethane dissolved in 10 ml dry tetraglyme was added to the flask portion wise and the mixture was heated to 70 °C. After overnight reaction at 70 °C, crude product was directly distilled out from reaction mixture under reduced pressure. Crude product was then distilled again with ∼0.1 g of NaH at ∼20 mbar (b.p. ∼47 °C) to receive 6.96 g (50% yield) pure product as a colorless liquid. iPrME (57% yield), iBME (33% yield), iPrEE (35% yield) and tBEE (29% yield) were synthesized following similar procedure using corresponding precursors shown in Fig. S2.

Synthesis of cPME and iPrBE.—In the example of cPME, to a round-bottom flask was added 29.4 g (2.0 eq.) sodium carbonate, 41.3 g (2.0 eq.) cyclopentyl bromide and 10.6 g (1.0 eq.) 2-methoxy ethanol. The mixture was stirred and heated up to 120 °C overnight. After cooling down, 100 ml diethyl ether was added followed by 100 ml of deionized water to dissolve all solid materials. The organic phase was separated, washed with 50 ml deionized water twice, 50 ml brine once and dried over anhydrous $MgSO_4$. After filtering, diethyl ether was removed under reduced pressure and the remaining was purified by flash column chromatography (EA/hexane, EA volume fraction 0–30%). The crude product was distilled with ∼0.1 g of NaH at ∼15 mbar (b.p. ∼60 °C) to receive 3.6 g (18% yield) of cPME product as a colorless liquid. iPrBE (52% yield) was synthesized from the reaction of 1-iodobutane and ethylene glycol mono-*iso*-propyl ether following similar procedure despite 0.6 eq. of KOH was added in addition to sodium carbonate and the reaction was heated for 3 days to push conversion.

Physical characterization.—Nuclear magnetic resonance (NMR) spectroscopy of synthesis product was performed on a Bruker Ascend 9.4 T/400 MHz instrument. Raman spectroscopy of electrolyte solution was performed on a HORIBA LabRAM HR Evolution Confocal Raman Microscope using glass chambers sealed in glovebox.[18] Differential scanning calorimetry (DSC) of electrolyte solution were performed with a TA Instruments Discovery 2500 differential scanning calorimeter. DSC sample was first pretreated by heating to 80 °C at 10 °C min^{-1} and held at 80 °C for 1 min (not shown), then cooled to −80 °C and looped back to 80 °C at 10 °C min^{-1}.[29] SEM of deposited lithium metal was performed on a Carl Zeiss Merlin Field Emission Scanning Electron Microscope. Lithium metal sample was retrieved from Cu/LFP cell after two formation cycles at C/10 and single charging at C/3. XPS was performed with a ThermoFisher Scientific XPS: NEXSA G2 instrument and etching was performed with a EX06 monatomic Ar ion source. Lithium metal sample was prepared by deposition in Li/Cu cell at a current density of 1 mA cm^{-2} to 1.5 mAh cm^{-2}. An air-tight transfer chamber was used to transfer sample from glovebox to XPS instrument without air exposure.

Electrochemical characterizations.— *Coin cell preparation.*—All the electrochemical characterizations except for lithium potential test were performed in CR2032 type coin cells. For cells tested below 4 V vs Li/Li^+, the following configuration was used: negative case‖spring‖spacer‖anode (counter electrode)‖25 μl electrolyte‖1 separator‖25 μl electrolyte‖cathode (working electrode)‖spacer‖positive case. For cells tested above 4 V vs Li/Li^+, a slightly modified configuration was used: negative case‖spring‖spacer‖spacer‖anode (counter electrode)‖25 μl electrolyte‖1 separator‖25 μl electrolyte‖cathode (working electrode)‖aluminum foil‖aluminum coated positive case.

General electrochemical tests.—EIS of stainless steel/stainless steel (SS/SS) cell was performed with a Biologic VSP-300 Potentiostat in 100 Hz to 7 MHz frequency range. Temperature was controlled from 80 °C to −60 °C in 10 degree intervals.[29] Celgard 2325 separator was used for all electrolytes and a cell constant of 12.4 calibrated by a Platinum-Cell Conductivity Probe (Vernier) was used. Lithium potential test was performed in Li/Pt beaker cells following procedures described in previous work.[18] Linear sweep voltammetry in Li/Al coin cell was performed at a scan rate of 1 mV s^{-1} from open circuit voltage to 6 V. For potentiostatic hold test and self-discharging test, Li/NMC811 coin cell was first charged to 4.4 V at a current rate of C/10 and cell voltage was held at 4.4 V for 3 h. Then the cell was rested for 48 h and open circuit voltage was recorded.

Simulations.— *Density functional theory (DFT) calculations.*—Oxidation potential was predicted by DFT calculations following procedures described in our previous work.[29]

Acknowledgments

This work was supported by the National Science Foundation (NSF) CAREER Award (CBET-2144454). This work made use of the shared facilities (Raman and SEM) at the University of Chicago Materials Research Science and Engineering Center, supported by the National Science Foundation under award number DMR-2011854. Parts of this work (DSC) were carried out at the Soft Matter Characterization Facility of the University of Chicago. NMR measurements were performed at the UChicago Chemistry NMR Facility. XPS was performed at The Northwestern University's Atomic and Nanoscale Characterization Experimental Center (NUANCE). The DFT calculations were performed with resources provided by the University of Chicago's Research Computing Center. The authors thank Steve Trask and Andrew Jansen at Argonne's Cell Analysis, Modeling, and Prototyping (CAMP) facility for providing electrodes.

ORCID

Peiyuan Ma https://orcid.org/0000-0003-0373-3712
Chibueze V. Amanchukwu https://orcid.org/0000-0002-6573-1213

References

1. K. Xu, "Nonaqueous liquid electrolytes for lithium-based rechargeable batteries." *Chem. Rev.*, **104**, 4303 (2004).
2. R. Schmuch, R. Wagner, G. Hörpel, T. Placke, and M. Winter, "Performance and cost of materials for lithium-based rechargeable automotive batteries." *Nat. Energy*, **3**, 267 (2018).
3. D. Lin, Y. Liu, and Y. Cui, "Reviving the lithium metal anode for high-energy batteries." *Nat. Nanotechnol.*, **12**, 194 (2017).
4. A. J. Louli et al., "Diagnosing and correcting anode-free cell failure via electrolyte and morphological analysis." *Nat. Energy*, **5**, 693 (2020).
5. S. Nanda, A. Gupta, and A. Manthiram, "Anode-free full cells: a pathway to high-energy density lithium-metal batteries." *Adv. Energy Mater.*, **11**, 2000804 (2021).
6. C. Niu et al., "Balancing interfacial reactions to achieve long cycle life in high-energy lithium metal batteries." *Nat. Energy*, **6**, 723 (2021).
7. J. Xiao et al., "Understanding and applying coulombic efficiency in lithium metal batteries." *Nat. Energy*, **5**, 561 (2020).
8. X. Cao et al., "Monolithic solid-electrolyte interphases formed in fluorinated orthoformate-based electrolytes minimize Li depletion and pulverization." *Nat. Energy*, **4**, 796 (2019).
9. Z. Zewen et al., "Capturing the swelling of solid-electrolyte interphase in lithium metal batteries." *Science (80-.)*, **375**, 66 (2022).
10. G. M. Hobold, K-H. Kim, and B. M. Gallant, "Beneficial vs inhibiting passivation by the native lithium solid electrolyte interphase revealed by electrochemical Li+ exchange." *Energy Environ. Sci.* (2023).
11. X. Ren et al., "Enabling high-voltage lithium-metal batteries under practical conditions." *Joule*, **3**, 1662 (2019).
12. R. Weber, M. Genovese, A. J. Louli, S. Hames, C. Martin, I. G. Hill, and J. R. Dahn, "Long cycle life and dendrite-free lithium morphology in anode-free lithium pouch cells enabled by a dual-salt liquid electrolyte." *Nat. Energy*, **4**, 683 (2019).
13. Z. Yu et al., "Molecular design for electrolyte solvents enabling energy-dense and long-cycling lithium metal batteries." *Nat. Energy*, **5**, 526 (2020).
14. Z. Yu et al., "Rational solvent molecule tuning for high-performance lithium metal battery electrolytes." *Nat. Energy*, **7**, 94 (2022).
15. S-J. Park, J-Y. Hwang, C. S. Yoon, H-G. Jung, and Y-K. Sun, "Stabilization of lithium-metal batteries based on the *in Situ* formation of a stable solid electrolyte interphase layer." *ACS Appl. Mater. Interfaces*, **10**, 17985 (2018).
16. D-J. Yoo, S. Yang, K. J. Kim, and J. W. Choi, "Fluorinated aromatic diluent for high-performance lithium metal batteries." *Angew. Chemie Int. Ed.* (2020), n/a (n/a).
17. P. Ma, P. Mirmira, P. J. Eng, S-B. Son, I. D. Bloom, A. S. Filatov, and C. V. Amanchukwu, "Co-intercalation-free ether electrolytes for graphitic anodes in lithium-ion batteries." *Energy Environ. Sci.*, **15**, 4823 (2022).
18. P. Ma, R. Kumar, M. C. Vu, K-H. Wang, P. Mirmira, and C. V. Amanchukwu, "Fluorination promotes lithium salt dissolution in borate esters for lithium metal batteries." *J. Mater. Chem. A*, **12**, 2479 (2024).
19. Z. Wang et al., "A new OECD definition for per- and polyfluoroalkyl substances." *Environ. Sci. Technol.*, **55**, 15575 (2021).
20. M. G. Evich et al., "Per- and polyfluoroalkyl substances in the environment." *Science (80-.)*, **375**, eabg9065 (2022).
21. Z. Li et al., "Non-polar ether-based electrolyte solutions for stable high-voltage non-aqueous lithium metal batteries." *Nat. Commun.*, **14**, 868 (2023).
22. E. Park et al., "Exploiting the steric effect and low dielectric constant of 1,2-Dimethoxypropane for 4.3 V lithium metal batteries." *ACS Energy Lett.*, **8**, 179 (2023).
23. Z. Wang, C. Chen, D. Wang, Y. Zhu, and B. Zhang, "Stabilizing interfaces in high-temperature NCM811-Li batteries via tuning terminal Alkyl Chains of ether solvents." *Angew. Chemie Int. Ed.*, **62**, e202303950 (2023).
24. K. Ding et al., "Tuning the solvent Alkyl Chain to tailor electrolyte solvation for stable Li-metal batteries." *ACS Appl. Mater. Interfaces* (2022).
25. J. Zhang, Q. Li, Y. Zeng, Z. Tang, D. Sun, D. Huang, Y. Tang, and H. Wang, "Weakly solvating cyclic ether electrolyte for high-voltage lithium metal batteries." *ACS Energy Lett.*, **8**, 1752 (2023).
26. W. A. Henderson, D. M. Seo, S-D. Han, and O. Borodin, "Electrolyte solvation and ionic association. VII. Correlating Raman spectroscopic data with solvate species." *J. Electrochem. Soc.*, **167**, 110551 (2020).
27. J. Wang, Y. Yamada, K. Sodeyama, C. H. Chiang, Y. Tateyama, and A. Yamada, "Superconcentrated electrolytes for a high-voltage lithium-ion battery." *Nat. Commun.*, **7**, 12032 (2016).
28. S. Ko, T. Obukata, T. Shimada, N. Takenaka, M. Nakayama, A. Yamada, and Y. Yamada, "Electrode potential influences the reversibility of lithium-metal anodes." *Nat. Energy* (2022).
29. P. Ma, P. Mirmira, and C. V. Amanchukwu, "Effect of building block connectivity and ion solvation on electrochemical stability and ionic conductivity in novel fluoroether electrolytes." *ACS Cent. Sci.*, **7**, 1232 (2021).
30. Y. Zhao, T. Zhou, T. Ashirov, M. E. Kazzi, C. Cancellieri, L. P. H. Jeurgens, J. W. Choi, and A. Coskun, "Fluorinated ether electrolyte with controlled solvation structure for high voltage lithium metal batteries." *Nat. Commun.*, **13**, 2575 (2022).
31. Y. Wang, W. Chen, Q. Zhao, G. Jin, Z. Xue, Y. Wang, and T. Mu, "Ionicity of deep eutectic solvents by walden plot and pulsed field gradient nuclear magnetic resonance (PFG-NMR)." *Phys. Chem. Chem. Phys.*, **22**, 25760 (2020).
32. B. D. Adams, J. Zheng, X. Ren, W. Xu, and J-G. Zhang, "Accurate determination of coulombic efficiency for lithium metal anodes and lithium metal batteries." *Adv. Energy Mater.*, **8**, 1702097 (2018).
33. S. C. Kim et al., "Potentiometric measurement to probe solvation energy and its correlation to lithium battery cyclability." *J. Am. Chem. Soc.* (2021).